

# PHYSICAL PROPERTIES OF THE MOLECULAR OUTFLOW IN HIGH-MASS STAR-FORMING REGION G240.31+0.07

JUNHAO LIU and KEPING QIU

*School of Astronomy & Space Science, Nanjing University, Nanjing, P.R.China*

## ABSTRACT

We present Atacama Pathfinder Experiment (APEX) CO (3-2), (6-5), and (7-6) observations toward massive star forming region G240.31+0.07. The integrated high velocity and low velocity emissions of three lines reveal a bipolar outflow and show similarity in morphology. Together with combined Submillimeter Array (SMA) and Caltech Submillimeter Observatory (CSO) 10.4 m telescope data in CO (2-1), by the means of Large Velocity Gradient (LVG) modeling and population diagram analysis, we explore the physical properties of the outflowing gas as a function of gas velocity. Our results reveal that the temperature of the outflowing gas has an almost constant value of  $\sim 50$  K. The constant trend is consistent with the isothermal assumption of the wide angle wind model. We also find a decreasing trend of CO column density with gas velocity. In addition, the modeling results reveal that the outflowing gas is thermalised and no upper limits to the gas density could be derived. The lower limits of gas density are  $n_{\text{low}} \sim 10^5 \text{ cm}^{-3}$  at most velocities.

*Subject headings:* ISM: individual (G240.31+0.07) - ISM: jets and outflows - stars: formation - stars: early-type

## 1. INTRODUCTION

Bipolar molecular outflows are ubiquitous around low-mass and high-mass young stellar objects (Lada 1985; Fukui et al. 1993; Zhang et al. 2001; Beuther et al. 2002; Maud et al. 2015). Theoretical work suggests that, in low-mass star formation, molecular outflows are related to disk-accretion process, and they play an important role in dissipating excess angular momentum of the infalling material (Shu et al. 1987; Bachiller 1996). However, due to the rarity and the typically larger distances, massive molecular outflows and their driving sources are not well studied as their low-mass counterparts. Thus, it is not clear how the massive outflows are accelerated, how they differ from low-mass outflows, and how they affect the star forming process. It is essential to address these questions by studying individual high-mass star forming regions.

Most previous studies of outflows have used low-excitation lines of CO, which are easily ex-

cited at low temperatures, to characterize relative cold molecular gas in morphology and kinematics (Qiu et al. 2009; Qiu & Zhang 2009; Qiu et al. 2011). Due to the lack of high-J CO line observations, multi CO line studies of outflow are very rare.

Here we report the 12-m submillimeter Atacama Pathfinder Experiment Telescope<sup>1</sup> (APEX) observations towards G240.31+0.07 (hereafter G240), an active high-mass star formation region which is associated with the IRAS 07427-2400 source and located at a distance of 5.41 kpc (Sakai et al. 2015). It harbors an ultracompact (UC) HII region and is reported to have OH and H<sub>2</sub>O maser emission (Hughes & MacLeod 1993; Caswell 1997; MacLeod et al. 1998; Migenes et al. 1999; Caswell 2003). Its far-infrared luminosity of  $10^{4.7} L_{\odot}$  is consistent with a O8.5 spectral type

<sup>1</sup>The Atacama Pathfinder Experiment Telescope is a collaboration between the Max-Planck-Institut für Radioastronomie, the European Southern Observatory, and the Onsala Space Observatory.

zero-age main-sequence (ZAMS) star (MacLeod et al. 1998). A near-infrared study have found two bright elongated  $\text{H}_2$  emission knots near the source (Kumar et al. 2002). Kumar et al. (2003) further argued that the shocked  $\text{H}_2$  emission indicates the presence of a massive rotating disk or envelope around the luminous YSO IRAS 07427-2400. There are also millimeter and centimeter radio continuum observations towards G240. Two clumps were detected by Chen et al. (2007) at 654 GHz ( $460 \mu\text{m}$ ), with clump A coinciding with a VLA 6 cm point source (Hughes & MacLeod 1993) and an  $\text{H}_2\text{O}$  maser. Qiu et al. (2009) presented a high resolution interferometric study at 1.3 mm and resolved the central part of G240 into three dusty cores MM1, MM2, and MM3, with the brightest core MM1 coinciding with the VLA 6 cm point source spatially. Trinidad (2011) presented observations at 1.3, 3.6, and 6 cm and reported radio continuum emission at the position of the three millimeter sources in at least one wavelength. G240 have also been mapped with single dish and interferometric observations in CO emission. High velocity CO (1-0) gas was detected towards G240 (McCutcheon et al. 1991; Shepherd & Churchwell 1996), tracing a bipolar outflow (Shepherd & Churchwell 1996). Hunter (1997) mapped the CO (3-2) emission with a  $20''$  beam and found a prominent bipolar outflow at a position angle (PA) of  $138^\circ$  and a weaker component at  $\text{PA} \sim 101^\circ$ . Kumar et al. (2003) also detected a prominent component and a weaker component of the bipolar CO (3-2) outflow with a  $20''$  beam and reported the PA of the prominent component to be  $132^\circ$ . Recently, Qiu et al. (2009) presented a detailed single dish and interferometric study of  $^{12}\text{CO}(2-1)$  and  $^{13}\text{CO}(2-1)$  emission and detected a bipolar, wide-angle, quasi-parabolic molecular outflow. In addition, Qiu et al. (2014) reported the detection of an hourglass magnetic field aligned within  $20^\circ$  of the outflow axis.

In this paper we present a CO multi transition (3-2, 6-5, 7-6) study towards the G240 outflow. With large velocity gradient (LVG) calculations and population diagram analysis, we explore the physical properties of the outflowing gas as a function of outflow velocity. We then discuss the results of the analysis.

## 2. OBSERVATIONS

The APEX observations were conducted on . CO (6-5) and CO (7-6) were observed simultaneously.

## 3. RESULTS

### 3.1. CO EMISSION

Figure 1 shows maps of the integrated low-velocity (LV) and high-velocity (HV) blueshifted and redshifted emissions of CO  $J = (3-2)$ , (6-5), (7-6) lines. For comparison, we integrate the LV and HV line wings of CO (3-2) and CO (6-5), as well as CO (7-6) LV emission, with the velocity range same as that in Qiu et al. (2009) Figure 2(a) and Figure 2(b), which is 58 to  $64 \text{ km s}^{-1}$  and 74 to  $80 \text{ km s}^{-1}$  for the LV blueshifted lobe and redshifted lobe, 42 to  $56 \text{ km s}^{-1}$  and 82 to  $94 \text{ km s}^{-1}$  for the HV blueshifted lobe and redshifted lobe, respectively. As the CO (7-6) observation is less sensitive than observations of CO (3-2) and CO (6-5), we integrate the HV emission of CO (7-6) with 50 to  $56 \text{ km s}^{-1}$  for the blueshifted lobe and 82 to  $88 \text{ km s}^{-1}$  for the redshifted lobe, to exclude channels which are dominated by noise. The outflow morphologies seen in three lines are very similar. For CO  $J = (3-2)$  and (6-5) emissions, a low-velocity and high-velocity prominent bipolar outflow is detected at position angle (PA)  $\sim 131^\circ$ , along with a low-velocity weaker component detected at  $\text{PA} \sim 101^\circ$ . However, the weaker outflow is not clearly seen in CO (7-6). It could result from the limited sensitivity of CO (7-6) observation. Due to the low resolution of our CO  $J = (3-2)$ , (6-5), (7-6) observations, we don't see the wide-angle structure reported by Qiu et al. (2009).

### 3.2. LINE RATIOS

For a proper comparison of different line emissions, we convolved the CO (6-5) and (7-6) maps, as well as the CO (2-1) map from Qiu et al. (2009), to the same spatial resolution of CO (3-2), which is  $19''$ . To reduce the noise level, we resampled the four CO lines to the resolution of  $2 \text{ km s}^{-1}$ . Then we measured the main beam temperature ratios of the four transitions toward the peak of the blueshifted and redshifted lobes (marked as two crosses in Figure 1). We adopted the cloud velocity ( $v_{\text{cloud}}$ ) from Kumar et al. (2003), which

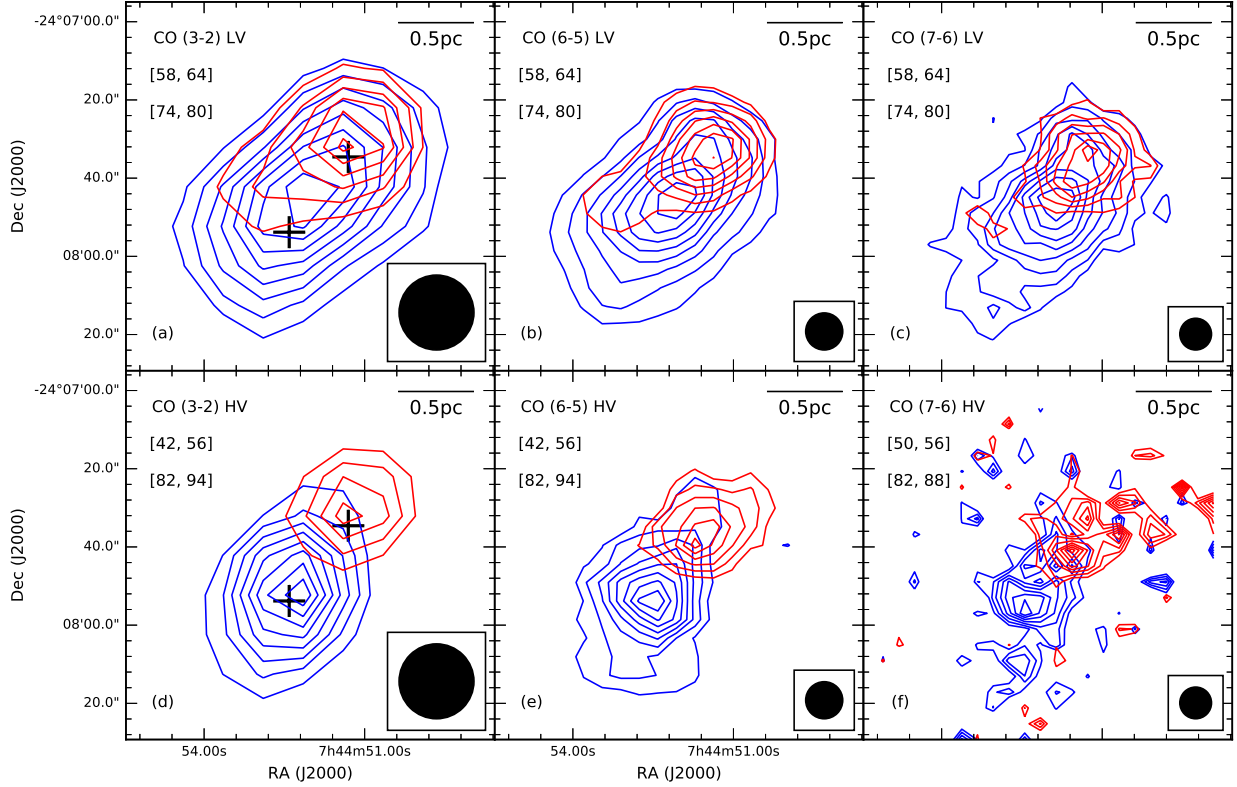


Fig. 1.— (a)-(c) Low-velocity emission of CO  $J = (3-2)$ ,  $(6-5)$ ,  $(7-6)$  lines, with velocity range 58 to 64 km s<sup>-1</sup> and 74 to 80 km s<sup>-1</sup> for the blueshifted lobe (blue) and the redshifted lobe (red); (d)-(e) High-velocity emission of CO  $J = (3-2)$ ,  $(6-5)$  lines, with velocity range 42 to 56 km s<sup>-1</sup> and 82 to 94 km s<sup>-1</sup> for the blueshifted lobe (blue) and the redshifted lobe (red); (f) High-velocity CO  $J = (7-6)$  emission, with velocity range 50 to 56 km s<sup>-1</sup> and 82 to 88 km s<sup>-1</sup> for the blueshifted lobe (blue) and the redshifted lobe (red). For (a)-(e), the contour levels are starting from 20% and at steps of 10%. For (f), the contour levels are starting from 30% and at steps of 10%. The central stars mark the position of the millimeter sources detected by Qiu et al. (2009). The beam size is shown in the lower right corner of each panel.

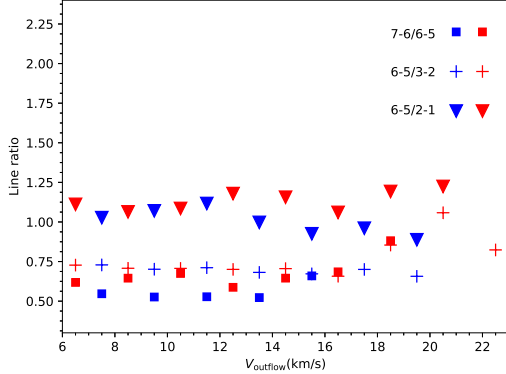


Fig. 2.— Ratios of main beam temperature of different CO lines versus outflowing gas velocity, as observed towards the blueshifted lobe (blue symbols) and the redshifted lobe (red symbols). The  $V_{\text{outflow}}$  shown here is the gas velocity with respect to the cloud velocity ( $v_{\text{cloud}}$ ):  $V_{\text{outflow}} = |v_{\text{observed}} - v_{\text{cloud}}|$ , where  $v_{\text{observed}}$  is the observed gas velocity.

is about  $67.5 \text{ km s}^{-1}$  with respect to the local standard of rest. Figure 2 shows the ratio-velocity distributions of the blueshifted gas and redshifted gas. All line ratios ((7-6)/(6-5), (6-5)/(3-2), (6-5)/(2-1)) appear to be almost constant at different velocities.

### 3.3. PHYSICAL PROPERTY ANALYSIS

We performed LVG analysis with the radiative transfer code RADEX developed by van der Tak et al. (2007). The simulation constructs a large grid of non-LTE models with three parameters: gas density ( $n_{\text{H}_2}$ ), kinetic temperature ( $T_{\text{kin}}$ ), and the ratio between column density and line width ( $N_{\text{CO}}/\Delta V$ ). Considering of the velocity resolution of our observations, we fix  $\Delta V$  to  $2 \text{ km s}^{-1}$ . Each model gives the prediction of the brightness temperature ( $T_{\text{b}}$ ) of different CO transitions. Then we measured the main beam temperature ( $T_{\text{mb}}$ ) of four CO lines extracted at the peak position of the blue lobe and red lobe (marked as two crosses in Figure 1). To compare the simulated  $T_{\text{b}}$  with our measured  $T_{\text{mb}}$ , we need to consider about the

beam dilution, as  $T_{\text{mb}}$  is related to  $T_{\text{b}}$ :

$$T_{\text{mb}} = \frac{\Omega_{\text{s}}^2}{\Omega_{\text{s}}^2 + \Omega_{\text{mb}}^2} \times T_{\text{b}} = f_{\text{b}} \times T_{\text{b}}, \quad (1)$$

where  $\Omega_{\text{s}}^2$  and  $\Omega_{\text{mb}}^2$  are the source size and the beam size in arcsec, and  $f_{\text{b}}$  is the beam filling factor. Given the complex structures of G240 outflow at higher resolution (Qiu et al. 2009), we can't get a good estimate of the source size. Then the beam filling factors are assumed to be the same for all transitions, and fixed to 1, during our analysis. Thus, the derived physical parameters of the gas are beam-averaged values. We further discuss how the beam dilution affect our results in the following part of this section.

We report the results from a  $\chi_{\text{red}}^2$  fitting.  $\chi_{\text{red}}^2$  is the reduced  $\chi^2$ :

$$\chi_{\text{red}}^2 = \frac{1}{N - n} \sum_{i=1}^4 (I_o - I_m)^2 / \sigma^2, \quad (2)$$

where  $N$  is the number of observed intensities,  $n$  the number of fitted parameters,  $I_o$  the observed intensity,  $I_m$  the modelled intensity, and  $\sigma$  is the uncertainty of the observed intensity. With four line observations and three simulation parameters, our fitting has one degrees of freedom. Considering the calibration error and pointing accuracy of our CO observations, we set the intensity uncertainty of CO (2-1), CO (3-2), CO (6-5), CO (7-6) to 0.15, 0.2, 0.25, 0.3 respectively. The best fit is then obtained by minimizing the  $\chi_{\text{red}}^2$  between the observed and modelled data using the Levenberg-Marquardt method (Press et al. 1992). However, in velocities where no CO (7-6) emission is detected, the best fit is obtained by minimizing  $\chi^2$  instead of  $\chi_{\text{red}}^2$ . Then we found the best fitting result at most velocities has a  $\chi_{\text{red}}^2$  less than 1, indicating that we might be a bit conservative at the intensity uncertainty or the real value of degrees of freedom is larger than one (Andrae et al. 2010). So we divided the intensity uncertainties by a appropriate factor to make  $\chi_{\text{red}}^2$  approach 1 at most velocities. At some velocities, the  $\chi_{\text{red}}^2$  remains much less than 1 even after our adjustment of intensity uncertainty, which can accounts for the anomaly high upper limits of gas temperature at these velocities in Figure 4(a).

In Figure 3, we show cuts in the  $\chi_{\text{red}}^2$  along the  $[T, n]$ ,  $[T, N]$ ,  $[n, N]$  planes for  $58 \text{ km s}^{-1}$  as

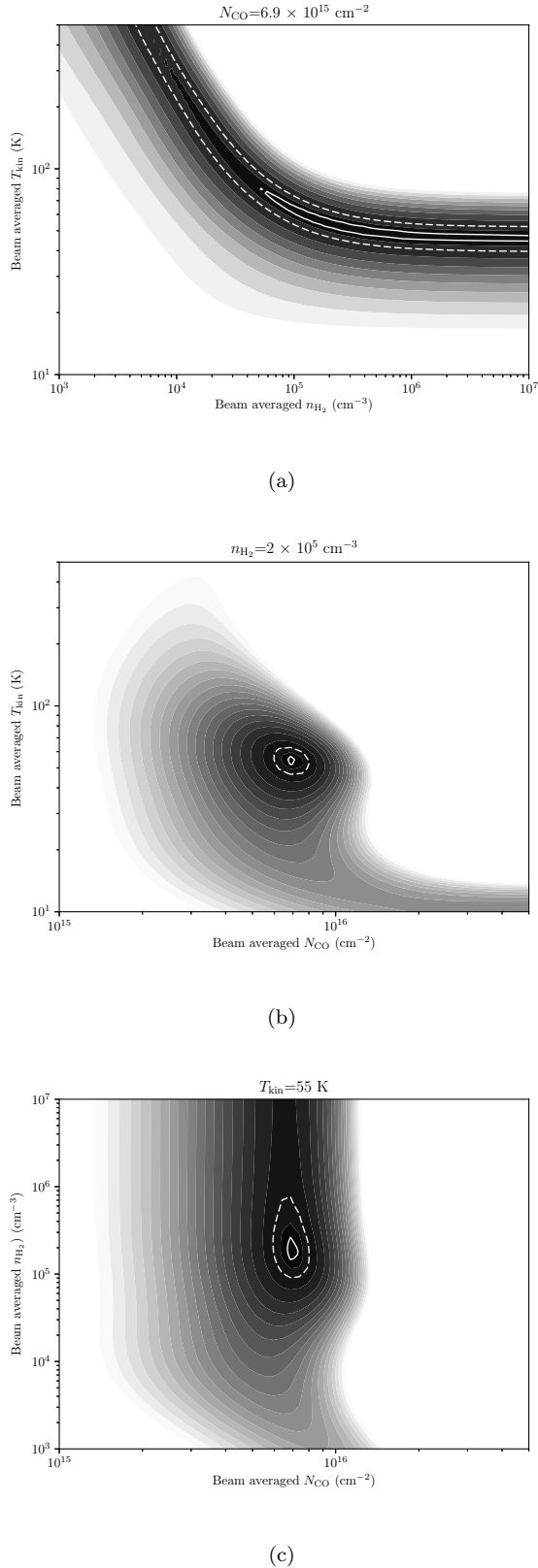


Fig. 3.— The  $\chi^2_{\text{red}}$  distribution for G240 outflow at  $58 \text{ km s}^{-1}$  in the (a)  $[T, n]$ , (b)  $[T, N]$ , (c)  $[n, N]$  planes, with all other parameters fixed to the parameters of the best fitting results at this velocity. Solid contours and dashed contours show the  $1\sigma$  and  $3\sigma$  confidence levels respectively.

an example of the  $\chi^2_{\text{red}}$  distribution, with all other parameters fixed to the parameters of the best fitting result at this velocity. The  $\chi^2_{\text{red}}$  distribution in  $[T, n]$ ,  $[T, N]$  planes is well behaved, with only one minimum, as shown in Figure 3(b) and Figure 3(c). However, Figure 3(a) shows that the gas might be thermalised and no upper limits to the density could be derived. The  $\chi^2_{\text{red}}$  distribution behaves similarly at other velocities.

We also performed a population diagram analysis with the assumption of local thermal equilibrium (LTE) and optically thin, and derived the kinetic temperature of the outflow gas and the CO column density as a function of velocity (Goldsmith & Langer 1999). Figure 4 shows the outflowing gas temperature and CO column density, estimated from the LVG analysis and population diagram analysis, versus outflowing gas velocity. The  $N$ - $V$  diagram shows a clear decreasing trend of CO column density with outflow velocity, while the  $T$ - $V$  diagram shows that the gas temperature has no obvious dependence on gas velocity. Uncertainty of each parameter in the LVG analysis is derived from the  $1\sigma$  confidence region in the  $N$ - $T$ - $n$  3-dimensional space. The  $1\sigma$  temperature uncertainty of the LVG analysis is shown in Figure 4(a), at velocities where all of the four lines are detected. The uncertainty of the CO column density is too small to be plotted, so we don't show it in Figure 4(b). The lower limits of gas density ( $n_{\text{lower}}$ ) are around  $10^5 \text{ cm}^{-3}$  at most velocities. At velocities where  $\chi^2_{\text{red}} \ll 1$ ,  $n_{\text{lower}}$  could be as low as  $3 \times 10^4 \text{ cm}^{-3}$ .

To explore how the effect of beam dilution influence our results, we varied the beam filling factors from 0.2 to 1. Then we performed the LVG analysis again, and compared the simulated  $T_b$  with the corrected antenna temperatures ( $T_{\text{mb}}$  divided by a beam filling factor). We find that modelling with different beam filling factors mainly affect the  $N$ - $V$  diagram, with minor change in the  $T$ - $V$  diagram and density limits. This could be resulted from the degeneracies of the beam filling factor with CO column density in the optically thin case.

## 4. DISCUSSION

### 4.1. Temperature

From the LVG analysis and the population diagram analysis, constant temperatures of  $\sim 50 \text{ K}$

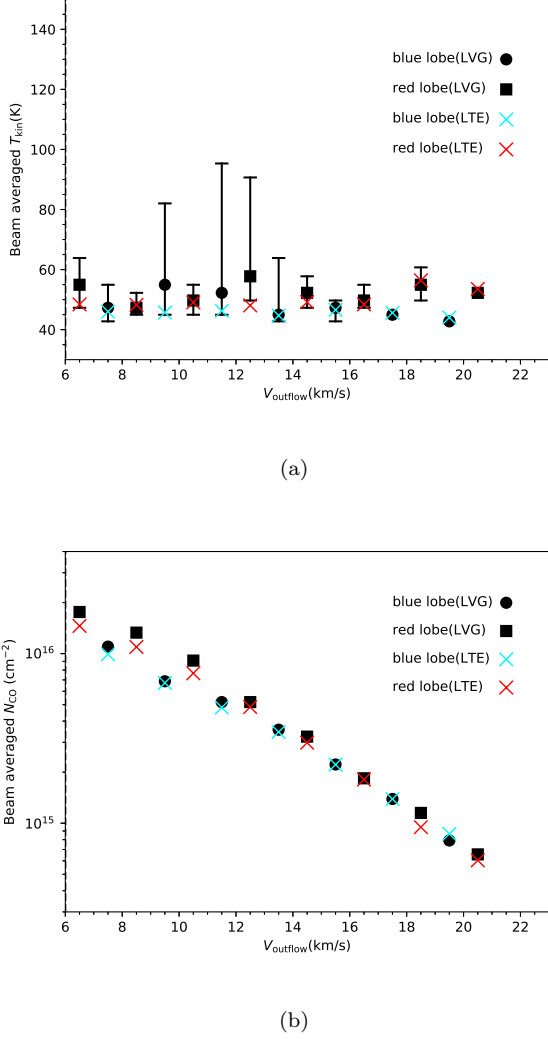


Fig. 4.—  $T-V$  and  $N-V$  diagram of the G240 outflow, estimated from LVG analysis (black circles for blue lobe and black squares for red lobe) and population diagram analysis (cyan x marker for blue lobe and red x marker for red lobe). The  $1\sigma$  temperature uncertainty estimated from the LVG analysis is represented in the  $T-V$  diagram (error bars).

are found for both the blue lobe and red lobe. This value is consistent with temperatures in excess of 50 K probed by van Kempen et al. (2016) for outflows associated with intermediate mass protostars, but slightly lower than temperatures estimated in outflows associated with low mass protostars (van Kempen et al. 2009; Yıldız et al. 2012).

With priori assumption of other parameters, the kinetic temperature of the outflowing gas can be derived from LVG analysis using two CO lines. Thus, the  $T - V$  relation in outflows can be studied. A rising trend of CO 3-2/6-5 ratio is observed towards the outflow gas associated with low mass YSO HH46 (van Kempen et al. 2009). If the density remains constant, the rising ratios observed at more extreme velocities could correspond to lower kinetic temperatures. In the case of outflowing gas toward low mass protostars NGC 1333 IRAS 4A and IRAS 4B, the CO 3-2/6-5 ratios are remarkably constant with velocity (Yıldız et al. 2012). With the assumption of constant density, the constant ratio trend shows little or no evidence of a temperature change with velocity. Based on CO (2-1) and CO (3-2) observations towards the extremely high velocity (EHV) outflow of high mass YSO G5.89-0.39, Su et al. (2012) assumed the canonical CO fractional abundance of  $10^{-4}$  and performed a LVG analysis, revealing a increasing trend of temperature with gas velocity. However, using the CO (6-5), (7-6) and (16-15) lines, Leurini et al. (2015) performed a rotation diagram analysis towards G5.89-0.39 outflow and found a decreasing trend of excitation temperature with increasing velocities. This disagreement seen in results of Su et al. (2012) and Leurini et al. (2015) could be due to different angular resolutions ( $3''.4$  compared to  $14''.5$ ). While Su et al. (2012) has smaller energy range covered by their CO line observations ( $\Delta E_u \sim 17$  K) compared to  $\Delta E_u \sim 600$  K of Leurini et al. (2015), the decreasing trend of temperature with velocity constrained in Leurini et al. (2015) is probably more appropriate for the G5.89-0.39 outflow. The different distributions of temperature with velocity reveal the complexity of molecular outflows.

In the wide-angle wind model, a molecular outflow is ambient material swept-up by a wide-angle radial wind. In previous numerical works, many authors have chosen isothermal equations for this model (Li & Shu 1996; Lee et al. 2001). Molecular

cooling dominates the cooling of the shocked material in the outflow at temperatures below  $10^4$  K (Hollenbach 1997). As the cooling rate increases as  $n^2$ , molecular cooling is very efficient for the density of a wind-driven outflow. Thus, an isothermal state could be reached in a wind-driven outflow, with no temperature change with velocity. This is consistent with our derivation of almost constant temperature in the massive G240 outflow. In addition, some other features of the molecular outflow associated with G240 can also be qualitatively interpreted by the wide-angle wind model (Qiu et al. 2009), while other outflow models have different predictions of these features, as reviewed by Arce et al. (2007). However, most outflow models existed have parameters typical of low mass outflows. It is necessary to compare the observational results of high mass outflows with models of similar physical conditions. Statics of outflows associated with high mass star forming regions are also essential for us to better understand the driven mechanism of massive outflows and the forming process of high mass stars.

#### 4.2. Density

The LVG analysis reveals that the lower limits of gas densities are  $\sim 10^5 \text{ cm}^{-3}$  at most velocities. We have found a decreasing trend of the beam averaged CO column density ( $N_{\text{CO,beam}}$ ) with gas velocity. As shown in Figure 4(b), for each velocity bin, the beam averaged CO column density drops from  $\sim 10^{16} \text{ cm}^{-2}$  to  $5 \times 10^{14} \text{ cm}^{-2}$  within  $15 \text{ km s}^{-1}$ . In the optically thin case, the beam averaged CO column density could be related to gas density  $n_{\text{H}_2}$ :

$$N_{\text{CO,beam}} = n_{\text{H}_2} \times \Delta V \times \frac{1}{dv/dr} \times X_{\text{CO}} \times f_b, \quad (3)$$

where  $f_b$  is the beam filling factor,  $X_{\text{CO}}$  the CO/H<sub>2</sub> abundance ratio,  $\Delta V$  the velocity interval and  $dv/dr$  is the velocity gradient. A drop in  $N_{\text{CO,beam}}$  at more extreme velocities indicates the decrease of one or several of these parameters.

As shown in Figure 3 of Qiu et al. (2009), the source size are  $\sim 20''$  and  $\sim 10''$  at velocities of  $\sim \pm 6 \text{ km s}^{-1}$  and  $\sim \pm 20 \text{ km s}^{-1}$  with respect to the cloud velocity, corresponding to beam filling factors of  $\sim 0.5$  and  $\sim 0.2$ , respectively. Considering the 2.5 times drop in the beam filling factor,

the 20 times drop in the beam averaged CO column density is consistent with  $\sim 8$  times decrease in the CO column density. As shown in Shu et al. (1995), estimation from an x-wind model predict the wind density decreasing with velocity and distance from the driving source. Thus, the decrease of gas density could interpret the decrease of CO column density with velocity. Due to the lack of further informations, we cannot assess whether the CO abundance ratio or the velocity gradient has attributed to the drop of CO column density at high velocities.

#### 5. SUMMARY

We have presented CO multi line observations toward high mass star forming region G240. With the LVG analysis, we have constrained the temperatures to  $\sim 50 \text{ K}$  and the H<sub>2</sub> density to values higher than  $n \sim 10^5 \text{ cm}^{-3}$  towards the outflow associated with G240. We also find a decreasing trend of CO column density with gas velocity.

#### REFERENCES

- Andrae, R., Schulze-Hartung, T., & Melchior, P. 2010, arXiv:1012.3754
- Arce, H. G., Shepherd, D., Gueth, F., et al. 2007, *Protostars and Planets V*, 245
- Bachiller, R. 1996, *ARA&A*, 34, 111
- Beuther, H., Schilke, P., Sridharan, T. K., et al. 2002, *A&A*, 383, 892
- Caswell, J. L. 1997, *MNRAS*, 289, 203
- Caswell, J. L. 2003, *MNRAS*, 341, 551
- Chen, H.-R., Su, Y.-N., Liu, S.-Y., et al. 2007, *ApJ*, 654, L87
- Fukui, Y., Iwata, T., Mizuno, A., Bally, J., & Lane, A. P. 1993, *Protostars and Planets III*, 603
- Goldsmith, P. F., & Langer, W. D. 1999, *ApJ*, 517, 209
- Hollenbach, D. 1997, *Herbig-Haro Flows and the Birth of Stars*, 182, 181
- Hughes, V. A., & MacLeod, G. C. 1993, *AJ*, 105, 1495

- Hunter, T. R. 1997, Ph.D. Thesis, 238
- Kumar, M. S. N., Bachiller, R., & Davis, C. J. 2002, *ApJ*, 576, 313
- Kumar, M. S. N., Fernandes, A. J. L., Hunter, T. R., Davis, C. J., & Kurtz, S. 2003, *A&A*, 412, 175
- Lada, C. J. 1985, *ARA&A*, 23, 267
- Lee, C.-F., Stone, J. M., Ostriker, E. C., & Mundy, L. G. 2001, *ApJ*, 557, 429
- Leurini, S., Wyrowski, F., Wiesemeyer, H., et al. 2015, *A&A*, 584, A70
- Li, Z.-Y., & Shu, F. H. 1996, *ApJ*, 472, 211
- MacLeod, G. C., Scalise, E., Jr., Saedt, S., Galt, J. A., & Gaylard, M. J. 1998, *AJ*, 116, 1897
- Maud, L. T., Moore, T. J. T., Lumsden, S. L., et al. 2015, *MNRAS*, 453, 645
- McCutcheon, W. H., Sato, T., Dewdney, P. E., & Purton, C. R. 1991, *AJ*, 101, 1435
- Migenes, V., Horiuchi, S., Slysh, V. I., et al. 1999, *ApJS*, 123, 487
- Press, W. H., Teukolsky, S. A., Vetterling, W. T., & Flannery, B. P. 1992, Cambridge: University Press, —c1992, 2nd ed.,
- Qiu, K., Zhang, Q., Wu, J., & Chen, H.-R. 2009, *ApJ*, 696, 66
- Qiu, K., & Zhang, Q. 2009, *ApJ*, 702, L66
- Qiu, K., Zhang, Q., & Menten, K. M. 2011, *ApJ*, 728, 6
- Qiu, K., Zhang, Q., Menten, K. M., et al. 2014, *ApJ*, 794, L18
- Sakai, N., Nakanishi, H., Matsuo, M., et al. 2015, *PASJ*, 67, 69
- Shepherd, D. S., & Churchwell, E. 1996, *ApJ*, 457, 267
- Shu, F. H., Adams, F. C., & Lizano, S. 1987, *ARA&A*, 25, 23
- Shu, F. H., Najita, J., Ostriker, E. C., & Shang, H. 1995, *ApJ*, 455, L155
- Su, Y.-N., Liu, S.-Y., Chen, H.-R., & Tang, Y.-W. 2012, *ApJ*, 744, L26
- Trinidad, M. A. 2011, *AJ*, 142, 147
- van der Tak, F. F. S., Black, J. H., Schöier, F. L., Jansen, D. J., & van Dishoeck, E. F. 2007, *A&A*, 468, 627
- van Kempen, T. A., van Dishoeck, E. F., Güsten, R., et al. 2009, *A&A*, 501, 633
- van Kempen, T. A., Hogerheijde, M. R., van Dishoeck, E. F., et al. 2016, *A&A*, 587, A17
- Yıldız, U. A., Kristensen, L. E., van Dishoeck, E. F., et al. 2012, *A&A*, 542, A86
- Zhang, Q., Ho, P. T. P., Wright, M. C. H., & Wilner, D. J. 1995, *ApJ*, 451, L71
- Zhang, Q., Hunter, T. R., Brand, J., et al. 2001, *ApJ*, 552, L167